# An Improved Depth-Averaged Non-Hydrostatic Shallow Water Model with Quadratic Pressure Approximation

Weizhi Wang*[1], Tobias Martin[1], Arun Kamath[1], and Hans Bihs[1]

[1]Department of Civil and Environmental Engineering, Norwegian University of Science and Technology (NTNU), 7491 Trondheim, Norway

*International journal for numerical methods in fluids*, 2020, , pp. .
DOI: http://dx.doi.org/10.1002/fld.4807

## Abstract

Phase-resolved information is necessary for many coastal wave problems, for example, for the wave conditions in the vicinity of harbour structures. Two-dimensional (2D) depth-averaging shallow water models are commonly used to obtain a phase-resolved solution near the coast. These models are in general more computationally effective compared to computational fluid dynamics (CFD) software and will be even more capable if equipped with a parallelised code. In the current paper, a 2D wave model solving the depth-averaged continuity equation and the Euler equations is implemented in the open-source hydrodynamic code REEF3D. The model is based on a non-hydrostatic extension and a quadratic vertical pressure profile assumption which provides a better approximation of the frequency dispersion. It is the first model of its kind to employ high-order discretisation schemes and to be fully parallelised following the domain decomposition strategy. Wave generation and absorption are achieved with a relaxation method. The simulations of non-linear long wave propagations and transformations over non-constant bathymetries are presented. The results are compared to benchmark wave propagation cases. A large-scale wave propagation simulation over realistic irregular topography is shown to demonstrate the model's capability of solving operational large-scale problems.

**Keywords:** wave modelling, numerical simulation, shallow water equations, dynamic pressure , quadratic profile

*Corresponding author,weizhi.wang@ntnu.no

*Postprint, published in International journal for numerical methods in fluids,* doi:http://dx.doi.org/10.1002/fld.4807

# 1 Introduction

Phase-resolved wave modelling is required for many applications in coastal engineering. It enables a time-domain analysis and presents more details for complex free-surface phenomena. Many efforts have been made to solve the Navier-Stokes equations for water waves with the fast development of computational infrastructures and the application of parallel computation techniques. Various methods have been used to capture the free-surface, such as the volume-of-fluid method Jacobsen et al. (2012); Higuera et al. (2013*a*); Hirt and Nichols (1981), the level set method Bihs et al. (2016); Osher and Sethian (1988) and the smooth particle hydrodynamics method Dalrymple and Rogers (2006); Altomare et al. (2017); Chow et al. (2019). Navier-Stokes solvers in combination with one of the aforementioned free-surface treatment methods are able to provide high-resolution results for complicated marine free-surface flows and near-field wave hydrodynamics. One example that is closely related to the current work is the open-source hydrodynamics model REEF3D. In Kamath et al. (2016), the solver was used to analyse non-breaking wave forces on various configurations of multiple vertical circular cylinders. Further simulations of marine fluid-structure interaction were performed for semi-submerged horizontal circular cylinders in tandem Ong et al. (2017), and non-linear marine hydrodynamics were investigated in detail Aggarwal et al. (2018). Broader applications of the model are also seen on the sediment transport analysis Ahmad et al. (2018) and the coastal infrastructure design Sasikumar et al. (2018). Typically, these simulations require relatively fine three-dimensional grids and are, therefore, more computationally demanding.

Phase-resolved modelling of the far-field wave field is important for delivering a realistic wave generation boundary condition for higher resolution near-field wave modelling. However, the far-field wave propagation towards the coast is a large-scale phenomenon, which puts a limitation on the application of the Navier-Stokes approach in spite of the increasing computational capacities. Less computationally demanding models are required to model the far-field large-scale phase-resolved wave propagation efficiently. As most coastal areas share relatively shallower water conditions, depth-averaged shallow water models have been favoured for the coastal wave modelling. These models are essentially two-dimensional and, thus, require less cells. The advances of such models have been focused on developing numerical methods to accurately capture the frequency dispersion relation and the non-linearity when the water depth increases or a rapidly varying bathymetry is involved. A common representative of shallow water models is the Boussinesq-type wave model Madsen et al. (1991); Nwogu (1993). Here, the lack of vertical flow information is compensated through the Boussinesq terms which help to calculate the correct frequency dispersion of the waves. This approach is valid from shallow to deep water, depending on the order of the Boussinesq terms Lynnett and Liu (200451). However, higher-order mixed time-space derivatives in the Boussinesq equations tend to cause numerical instabilities. More recently, the possibility of using non-hydrostatic shallow equations with a single layer or multiple layers in the vertical direction has been explored by Zijlema and Stelling Stelling and Zijlema (2003); Zijlema et al. (2005); Zijlema and Stelling (2008); Zijlema et al. (2011*a*). With an increasing number of vertical layers, the flow information in the vertical direction is better resolved. However, it has been shown previously that the increase of vertical layers leads to a significant increase in computational costs. For example, Monteban (2016) observed that the simulation time using two layers is nearly 10 times compared to that using a single layer. Cui et al. (2014) improved the two-layer approach such that it has similar computational efficiency as a one-layer counterpart and, yet,

maintaining a high linear dispersion accuracy. While the commonly used vertical pressure profile is linear, a quadratic pressure approach has been presented by Jeschke et al. (2017). It is stated that, with an approximation of a proposed quadratic vertical pressure profile, the model can achieve at least a good equivalence to existing fully non-linear weakly dispersive Boussinesq models Jeschke et al. (2017). This method presents itself as an attractive alternative for modelling shallow water waves, while potentially avoiding the numerical instabilities due to higher-order terms in a Boussinesq-type model and the increased computational costs from a larger number of vertical layers in a multi-layer non-hydrostatic model. However, only simple scenarios such as one-dimensional (1D) standing waves and progressive solitary waves over a flat bottom have been investigated previously Jeschke et al. (2017). Here, several terms of the derived equations are neglected which leaves the final question of reliability open. It is reported by Jeschke (2018) that it is challenging to incorporate the vital term involving the varying bathymetry into her numerical model. As a result, the model's accuracy is seen to be less ideal than the theoretical expectations when changing bottom is present. Therefore, this paper includes a numerical procedure to discretise this term appropriately. This enables the authors to emphasise the accuracy gain from the quadratic pressure approximation for non-constant bathymetries.

The accuracy of shallow water models has been improved over the last years. High-order numerical schemes are employed in the development of Boussinesq-types models. Wei and Kirby (1995) applied a $4^{th}$-order accurate Adams–Bashforth–Moulton (ABM) scheme for the time discretisation and a mixed $4^{th}$-order and $2^{nd}$-order scheme for the spatial discretisation. Shi et al. (2012) employed a mixed finite volume and finite difference method using a $4^{th}$-order accurate MUSCL (Monotone Upstream-centered Schemes for Conservation Laws) reconstruction technique for the advection term and a $3^{rd}$-order Runge-Kutta scheme for temporal discretisation. However, few high-order implementations are presented for non-hydrostatic models. Zijlema et al. (2011*b*) present their model using a $2^{nd}$-order discretisation scheme in space and a $2^{nd}$-order leapfrog algorithm in time. Jeschke et al. (2017) implement the quadratic pressure model with the $2^{nd}$-order ${P_1}^{NC} - P_1$ finite element method Hanert et al. (2005); Roux and Pouliot (2008) for the advection terms and a Leapfrog method for the time stepping. In a recent development, Jeschke (2018) also implemented a $2^{nd}$-order discontinuous Galerkin scheme in the model. Thus, high-order numerical implementations are left to be fulfilled in order to advance the development of non-hydrostatic models.

In addition, parallel computations are incorporated in many shallow water models in case of computationally demanding simulations. Shi et al. (2012) presents a parallelized Boussinesq model following the domain decomposition strategy with a Message Passing Interface (MPI). Good scaling characteristic is observed up to 48 cores. Zijlema et al. (2011*b*) also uses the same parallelisation technique and achieve linear scalability up to 8 cores. However, the newly proposed quadratic pressure approximation Jeschke et al. (2017) has not been incorporated into any parallel code. A good scalability up to hundreds of processors is also not presented in the literature regarding shallow water models in general. For large-scale operational engineering applications, such scalability is in great demand.

Ensuring high-quality input waves is another important aspect in the development of a shallow water model. The typical practice is to impose the surface elevation and the depth-averaged velocities to the boundary Madsen et al. (1991); Nwogu (1993); Wei et al. (1995); Zijlema et al. (2011*b*); Shi et al. (2012); Chen et al.. Periodic boundary conditions are also widely used, for example, a spatial periodic boundary condition is applied by Madsen et al.

(2002), and a double periodic boundary condition is implemented in Jeschke et al. (2017). Another popular wave generation method is the relaxation method Mayer et al. (1998); Jacobsen et al. (2012) which has high flexibility and tends to result in less reflected waves Miquel et al. (2018). This method has been widely implemented in Navier-Stokes solvers Azimi et al. (2014) but remains absent in the development of shallow water models. The feasibility of using a relaxation method for the wave generation and absorption in a non-hydrostatic shallow water model remains to be explored.

In the presented paper, REEF3D::SFLOW is introduced as a novel non-hydrostatic shallow water model following the quadratic pressure approximation Jeschke et al. (2017). Developed as a part of the REEF3D framework, the proposed model has direct access to all the existing numerical schemes and parallelisation algorithms in REEF3D. Thus, the model presents itself as the first non-hydrostatic shallow water model with high-order discretisation schemes, for example, a $5^{th}$-order Weighted-Essentially-Non-Oscillatory (WENO) scheme in spatial discretisation and a $3^{rd}$ to $4^{th}$-order Runge-Kutta scheme for the temporal discretisation. The model also innovatively employs the relaxation method Jacobsen et al. (2012) for the wave generation and absorption. With a model equipped with high-order numerical methods, this paper presents for the first time the simulations of non-linear long wave propagations over varying bathymetries using the quadratic pressure approximation. In these simulations, the equations with the depth-related terms are solved and the overall performance gain from the quadratic pressure approximation is investigated comprehensively. Computational scalability up to multi-hundred cores is demonstrated with the proposed model. An expanded validation process is then presented, including several well-known benchmark cases incorporating wave propagation over changing topographies and wave-structure interactions. Additionally, a large-scale coastal wave propagation over a natural topography is presented to demonstrate the model's capability for engineering applications.

## 2 Numerical Theory

The mass and momentum conservation for an incompressible inviscid flow leads to the continuity and Euler equations in three dimensions:

$$\frac{\partial U}{\partial x} + \frac{\partial V}{\partial y} + \frac{\partial W}{\partial z} = 0, \tag{1}$$

$$\frac{\partial U}{\partial t} + U\frac{\partial U}{\partial x} + V\frac{\partial U}{\partial y} + W\frac{\partial U}{\partial z} = -\frac{1}{\rho}\frac{\partial P_T}{\partial x}, \tag{2}$$

$$\frac{\partial V}{\partial t} + U\frac{\partial V}{\partial x} + V\frac{\partial V}{\partial y} + W\frac{\partial V}{\partial z} = -\frac{1}{\rho}\frac{\partial P_T}{\partial y}, \tag{3}$$

$$\frac{\partial W}{\partial t} + U\frac{\partial W}{\partial x} + V\frac{\partial W}{\partial y} + W\frac{\partial W}{\partial z} = -\frac{1}{\rho}\frac{\partial P_T}{\partial z} - g. \tag{4}$$

where $U$, $V$ and $W$ are velocities in x, y and z directions, $\rho$ is the constant density, $P_T$ represents the total pressure and $g$ is the gravitational acceleration. Additional source terms such as bottom friction and turbulent stresses are omitted here but are straightforward to include if needed.

The water depth $h = d+\zeta$ consists of two parts: the still water depth $d$ and the free-surface elevation $\zeta$, as displayed in Fig. 1. Defining the horizontal velocity vector as $\boldsymbol{U} = (U, V)$, the

kinematic boundary conditions at the free-surface and the bottom are:

$$W|_\zeta = \frac{\partial \zeta}{\partial t} + \boldsymbol{U}|_\zeta \cdot \nabla \zeta, \tag{5}$$

$$W|_{-d} = -\boldsymbol{U}|_{-d} \cdot \nabla d. \tag{6}$$

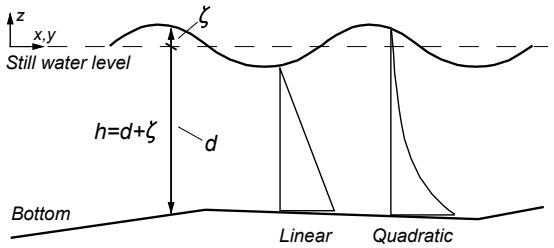


Figure 1: Basic definitions in the shallow water model: the water depth $h$, the still water depth $d$, the free-surface elevation $\zeta$, the coordinates system and the schematics of the assumed linear pressure profile and quadratic pressure approximation

The shallow water assumption, i.e. the horizontal acceleration is much greater than the vertical acceleration, implies a hydrostatic pressure. In order to get a hydrodynamic pressure correction, the total pressure $P_T$ is assumed to consist of a hydrostatic part $P$ and a hydrodynamic part $Q$. The pressure and its boundary condition at the free-surface is given by:

$$P_T = P + Q = \rho g(\zeta - z) + Q, \tag{7}$$

$$P_T|_\zeta = P|_\zeta = Q|_\zeta = 0. \tag{8}$$

The velocities and the dynamic pressure are depth-averaged by integrating over the water depth:

$$\boldsymbol{u} = (u, v) = \frac{1}{h}\int_{-d}^{\zeta} \boldsymbol{U}\,\mathrm{d}\,z; \quad w = \frac{1}{h}\int_{-d}^{\zeta} W\,\mathrm{d}\,z; \quad q = \frac{1}{h}\int_{-d}^{\zeta} Q\,\mathrm{d}\,z \tag{9}$$

In contrast to previous models Zijlema et al. (2011*b*), where the pressure is solved at the bottom, the proposed model consists of only depth-averaged quantities. A relation between the depth-averaged pressure $q$ and the pressure at the bottom $Q|_{-d}$ needs to be defined in order to close the system. If the linear pressure profile Stelling and Zijlema (2003); Zijlema et al. (2011*b*) is assumed, the pressure at the bottom is simply twice the depth-averaged pressure, or:

$$Q|_{-d} = 2q. \tag{10}$$

Consequently, the governing equations with only depth-averaged variables are:

$$\frac{\partial \zeta}{\partial t}+\frac{\partial hu}{\partial x}+\frac{\partial hv}{\partial y}=0, \tag{11}$$

$$\frac{\partial u}{\partial t}+u\frac{\partial u}{\partial x}+v\frac{\partial u}{\partial y}=-g\frac{\partial \zeta}{\partial x}-\frac{1}{\rho h}\left(\frac{\partial hq}{\partial x}-2q\frac{\partial d}{\partial x}\right), \tag{12}$$

$$\frac{\partial v}{\partial t}+u\frac{\partial v}{\partial x}+v\frac{\partial v}{\partial y}=-g\frac{\partial \zeta}{\partial y}-\frac{1}{\rho h}\left(\frac{\partial hq}{\partial y}-2q\frac{\partial d}{\partial y}\right), \tag{13}$$

$$\frac{\partial w}{\partial t}+u\frac{\partial w}{\partial x}+v\frac{\partial w}{\partial y}=-\frac{2q}{\rho h}. \tag{14}$$

Jeschke et al. (2017) replaces the linear assumption with a quadratic vertical pressure profile as shown in Eqn. (15).

$$Q|_{-d}=\frac{3}{2}q+\frac{1}{4}\rho h\Phi, \tag{15}$$

$$\Phi=-\nabla d\cdot(\partial_t \boldsymbol{u}+(\boldsymbol{u}\cdot\nabla)\boldsymbol{u})-\boldsymbol{u}\cdot\nabla(\nabla d)\cdot\boldsymbol{u}. \tag{16}$$

Following the quadratic assumption, the governing equations with depth-averaged variables become:

$$\frac{\partial \zeta}{\partial t}+\frac{\partial hu}{\partial x}+\frac{\partial hv}{\partial y}=0, \tag{17}$$

$$\frac{\partial u}{\partial t}+u\frac{\partial u}{\partial x}+v\frac{\partial u}{\partial y}=-g\frac{\partial \zeta}{\partial x}-\frac{1}{\rho h}\left(\frac{\partial hq}{\partial x}-\left(\frac{3}{2}q+\frac{1}{4}\rho h\Phi\right)\frac{\partial d}{\partial x}\right), \tag{18}$$

$$\frac{\partial v}{\partial t}+u\frac{\partial v}{\partial x}+v\frac{\partial v}{\partial y}=-g\frac{\partial \zeta}{\partial y}-\frac{1}{\rho h}\left(\frac{\partial hq}{\partial y}-\left(\frac{3}{2}q+\frac{1}{4}\rho h\Phi\right)\frac{\partial d}{\partial y}\right), \tag{19}$$

$$\frac{\partial w}{\partial t}+u\frac{\partial w}{\partial x}+v\frac{\partial w}{\partial y}=\frac{1}{\rho h}\left(\frac{3}{2}q+\frac{1}{4}\rho h\Phi\right). \tag{20}$$

The governing equations with the boundary conditions are solved on a structured staggered grid using a finite difference method (FDM). Chorin's projection method Chorin (1968) is applied for the solution of the velocities. The $5^{th}$-order conservative finite difference Weighted-Essentially-Non-Oscillatory (WENO) scheme proposed by Jiang and Shu (1996) is used for the discretisation of convective terms for the velocities $u$,$v$ and $w$. The Total-Variation-Diminishing (TVD) $3^{rd}$-order Runge-Kutta explicit time scheme developed by Shu and Osher (1988) is employed for time discretisation. It involves the calculation of the spatial derivatives and the dynamics pressure three times per time step. The information containing pressure is solved using the Poisson equation:

$$\frac{h_p}{\rho}\left(\frac{\partial^2 q}{\partial x^2}+\frac{\partial^2 q}{\partial y^2}\right)+\frac{2q}{\rho h_p}=\frac{1}{\partial x\partial t}\left(-h_p\left(\frac{\partial u}{\partial x}+\frac{\partial v}{\partial y}\right)-2w-u\frac{\partial d}{\partial x}-v\frac{\partial d}{\partial y}\right) \tag{21}$$

Here, the parameter $h_p$ denotes the water level in the centre of the cell. In a staggered grid arrangement, this is where the dynamic pressure $q$, the vertical velocities $w$ and the free surface location $\zeta$ are solved. The horizontal velocities are solved at the faces of the cells. The high-performance solver library HYPRE hyp (2015) is employed to solve the Poisson pressure equation using the PFMG-preconditioned BiCGStab algorithm Ashby and Flagout

(1996). The dynamic pressure $q$ is then used to correct the velocities in a correction step. Hence, the corrections of the velocities with the quadratic pressure approximation are

$$u^{n+1} = u^* + \Delta t \left( \frac{3}{2} \frac{q^{n+1}}{\rho h_p} \frac{\partial d}{\partial x} + \frac{1}{4} \Phi \frac{\partial d}{\partial x} \right), \tag{22}$$

$$v^{n+1} = v^* + \Delta t \left( \frac{3}{2} \frac{q^{n+1}}{\rho h_p} \frac{\partial d}{\partial y} + \frac{1}{4} \Phi \frac{\partial d}{\partial y} \right), \tag{23}$$

$$w^{n+1} = w^* + \Delta t \left( \frac{3}{2} \frac{q^{n+1}}{\rho h_p} + \frac{1}{4} \Phi \right). \tag{24}$$

where $u^*, v^*, w^*$ are intermediate-step velocities with only hydrostatic pressure.

The term $\Phi$ on the right-hand side of Eqn. (18) to Eqn. (20) is treated with a procedure following the principles of the fractional step method of Le and Moin (1991). Assuming the dynamic pressure does not change significantly within one Runge-Kutta sub-step, the intermediate velocities $u^*, v^*, w^*$ are corrected with the dynamic pressure gradients of the previous sub-step:

$$u^{**} = u^* - \frac{\partial q^{n,rk}}{\partial x}, \tag{25}$$

$$v^{**} = v^* - \frac{\partial q^{n,rk}}{\partial y}, \tag{26}$$

$$w^{**} = w^* - \frac{\partial q^{n,rk}}{\partial z}, \tag{27}$$

where $q^{n,rk}$ is the dynamic pressure from the previous Runge-Kutta sub-step. The spatial derivatives of $\Phi$ are updated with the corrected velocities $u^{**}, v^{**}$ and $w^{**}$ in equation Eqn. 16, which is then inserted into Eqn. (22) to Eqn. (24) to obtain the velocities at the new time step. The time derivative term inside $\Phi$ is then calculated with simple finite differences:

$$\partial_t \boldsymbol{u} = \frac{u^{**} - u^{n,rk}}{\alpha \Delta t}, \tag{28}$$

$$\partial_t \boldsymbol{v} = \frac{v^{**} - v^{n,rk}}{\alpha \Delta t}, \tag{29}$$

$$\partial_t \boldsymbol{w} = \frac{w^{**} - w^{n,rk}}{\alpha \Delta t}, \tag{30}$$

$$\tag{31}$$

where $\alpha$ is the increment factor of the corresponding Runge-Kutta sub-step and $u^{n,rk}, v^{n,rk}, w^{n,rk}$ are the velocities from the previous Runge-Kutta sub-step.

Parallel computation is enabled by decomposing the simulation domain into smaller sub-domains. The communication between these domains is achieved through a ghost cell approach. The message passing interface (MPI) is then used for the communication at the sub-domain boundaries.

The location of the free-surface $\zeta$ is determined based on the divergence of the depth-integrated horizontal velocities as given in Eqn. (17). The free-surface is reconstructed using the $5^{th}$-order WENO scheme Jiang and Shu (1996). The solutions of the stencils are weighted, i.e. a coefficient or weight is assigned to the solution of each stencil. The scheme assigns the largest weight to the smoothest solution and can therefore handle large-gradient free-surface changes caused by the varying bathymetry. As an example, the discretised form of Eqn. (17) in x-direction is presented in Eqn. (32).

$$\frac{\zeta_i^{n+1} - \zeta_i^n}{\triangle t} + \frac{\widehat{h}_{i+1/2}^n u_{i+1/2}^{n+1/2} - \widehat{h}_{i-1/2}^n u_{i-1/2}^{n+1/2}}{\triangle x} = 0, \tag{32}$$

where $\widehat{h}_{i+1/2}$ is the water level at the cell face $i + 1/2$. $\widehat{h}_{i+1/2}$ is reconstructed with the WENO procedure:

$$\widehat{h}_{i+1/2}^{\pm} = \omega_1^{\pm}\widehat{h}_{i+1/2}^{1\pm} + \omega_2^{\pm}\widehat{h}_{i+1/2}^{2\pm} + \omega_3^{\pm}\widehat{h}_{i+1/2}^{3\pm}. \tag{33}$$

The $\pm$ sign indicates the upwind direction. The nonlinear weights $\omega_n^{\pm}$ are calculated for each ENO stencil based on the smoothness indicators Jiang and Shu (1996). For the upwind direction in the positive $i$-direction, the three possible ENO stencils $\widehat{h}^1$, $\widehat{h}^2$ and $\widehat{h}^3$ are:

$$\widehat{h}_{i+1/2}^{1-} = \frac{1}{3}h_{i-2} - \frac{7}{6}h_{i-1} + \frac{11}{6}h_i, \tag{34}$$

$$\widehat{h}_{i+1/2}^{2-} = -\frac{1}{6}h_{i-1} + \frac{5}{6}h_i + \frac{1}{3}h_{i+1}, \tag{35}$$

$$\widehat{h}_{i+1/2}^{3-} = \frac{1}{3}h_i + \frac{5}{6}h_{i+1} - \frac{1}{6}h_{i+2}. \tag{36}$$

Wetting and drying are handled by setting the velocities in cells below a certain user-defined threshold of the water level to zero:

$$\begin{cases} u = 0, & if\ \widehat{h}_x < threshold, \\ v = 0, & if\ \widehat{h}_y < threshold. \end{cases} \tag{37}$$

The default threshold is set to be 0.00005 m, which is used throughout the presented work. The approach tracks the variation of the shoreline accurately and avoids numerical instabilities by ensuring non-negative water depth Stelling and Duinmeijer (2003); Zijlema and Stelling (2008).

Wave generation and absorption are carried out with the relaxation method as described in Bihs et al. (2016). The relaxation function formulated by Jacobsen Jacobsen et al. (2012) is used in the proposed model:

$$\Gamma(\widetilde{x}) = 1 - \frac{e^{(\widetilde{x}^{3.5})} - 1}{e - 1}\ for\ \widetilde{x} \in [0; 1], \tag{38}$$

where $\widetilde{x}$ is scaled to the length of the relaxation zone. The velocities $u, v$, the surface elevation $\zeta$ and the pressure $p$ are increased to the analytical values in the wave generation zone and reduced to zero or initial still wave values in the wave energy dissipation zone:

$$u(\widetilde{x})_{relaxed} = \Gamma(\widetilde{x})u_{analytical} + (1 - \Gamma(\widetilde{x}))u_{computational}, \tag{39}$$

$$v(\widetilde{x})_{relaxed} = \Gamma(\widetilde{x})v_{analytical} + (1 - \Gamma(\widetilde{x}))v_{computational}, \tag{40}$$

$$\zeta(\widetilde{x})_{relaxed} = \Gamma(\widetilde{x})\zeta_{analytical} + (1 - \Gamma(\widetilde{x}))\zeta_{computational}, \tag{41}$$

$$p(\widetilde{x})_{relaxed} = \Gamma(\widetilde{x})p_{analytical} + (1 - \Gamma(\widetilde{x}))p_{computational}. \tag{42}$$

All types of wave theories, type of wavemakers and wave signal input available in the existing code are applicable to the proposed shallow water model as well.

A breaking wave criterion is introduced The SWASH Team (2017) to represent the wave breaking process. The wave breaking is initialised when the vertical velocity of the free-surface exceeds a fraction of the shallow water celerity:

$$\frac{\partial \zeta}{\partial t} > \alpha \sqrt{gh}. \tag{43}$$

At the same time, the dynamic pressure is neglected and remains so at the front of the breaker. For the persistence of the wave breaking, the coefficient $\beta$ ($0 < \beta < \alpha$) is introduced in Eqn. (43) instead of $\alpha$ to stop the wave breaking process. The computations become non-hydrostatic again when the vertical velocity of the free-surface falls out of the range of the criterium. $\alpha = 0.6$ and $\beta = 0.3$ are recommended as they work well with most of the waves The SWASH Team (2017). By introducing the wave breaking criterion and removing the dynamic pressure during breaking, the momentum is well conserved, the energy dissipation is well represented and the asymmetry and skewness of non-linearity are respected The SWASH Team (2017).

# 3 Verification

The proposed numerical model REEF3D::SFLOW is first verified for the wave propagation in a 28 m long one-dimensional flume as shown in Fig. 2. The wave generation zone of one wavelength is at the inlet of the flume, and a wave energy dissipation zone of two wavelengths is located at the outlet. Four different wave cases are simulated with the proposed model.

## 3.1 Linear progressive wave propagation over constant bathymetry

First, a linear wave Dean and Dalrymple (1991*b*) of wave height $H = 0.02$ m and wavelength $L = 4$ m is simulated for 60 s. The water depth is constant at 0.5 m, correspondingly $kd = 0.25\pi$. A grid convergence study is initially performed with the cell sizes of 0.01 m, 0.02 m, 0.04 m and 0.08 m. Only one cell exits in the y-direction and its size equals to that in the x-direction. The Courant-Friedrichs-Lewy ($CFL$) number is kept constant at 0.2 for all cases. The wave profiles obtained using different cell sizes at $t = 90$ s are compared in Fig. 3a. As can be seen, $dx = 0.04$ m and $dx = 0.08$ m under-predict the wave height and show minor phase differences. The cell size of $dx = 0.02$ m represents the wave propagation sufficiently well, with a similar result as $dx = 0.01$ m. The average wave heights of the last ten wave periods in the time series at the wave gauge at $x = 14.5$ m from the inlet boundary are used to quantify the grid convergence property. The relative error between the averaged wave height and the theoretical value together with the L2 norm of the absolute errors are summarised in Table 2. A monotonic reduction of the error can be observed with the refinement of the grids.

Further, a series of simulations are performed with different $CFL$ numbers of 0.1, 0.2, 0.3 and 0.4 to investigate the impact of the time step. For this purpose, a constant cell size of 0.02 m is utilized. The different wave profiles at $t = 90$ s are compared in Fig. 3b. All tested $CFL$ numbers represent the phase information well in comparison to the theoretical wave. For $CFL = 0.3$ and 0.4, the wave height seems to reduce. The wave height information is better represented for $CFL = 0.1$ and 0.2, while an over-estimation of wave crest is noticed

with $CFL = 0.1$ in the chosen time frame. The relative errors and the L2 norms of errors are summarised in Table 1. $CFL$ number of 0.2 matches both the trough and crest well and errors approach to the ones with $CFL$ number 0.1. As a result, $CFL = 0.2$ will be used in all the following simulations of this paper. Fig. 4a shows that the linear progressive wave is well represented by the solver at an intermediate water depth. Both, the wave height and phase are matching satisfactorily. It is also noticeable that the relaxation method dissipates the wave energy well at the wave energy dissipation zone where the surface elevation remains constant at the still water level and no artificial reflection is observed.

The advantage of the quadratic pressure approximation is demonstrated by comparing the surface elevation with quadratic pressure approximation with the linear pressure profile in Stelling and Zijlema (2003); Zijlema et al. (2011*b*) (see Fig. 4b). It is observed that, with a linear pressure assumption, the wave phase starts to shift shortly after the waves propagate outside the generation zone. In contrast, the quadratic pressure approximation improves the phase accuracy significantly and approximates the theoretical value more precisely due to a better representation of dispersion.

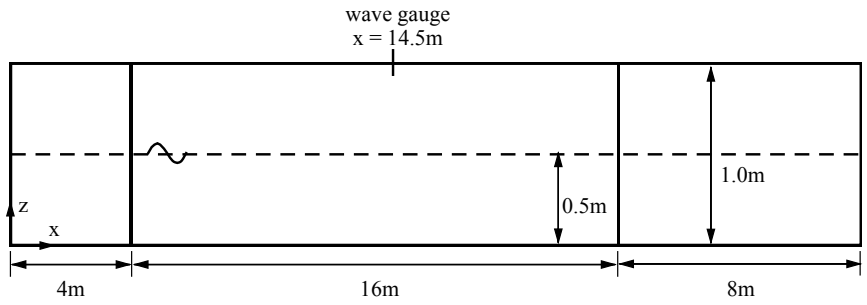


Figure 2: The numerical wave tank set-up of the 1D flume for linear progressive waves, view from the side. The left-hand side is the wave generation zone of one wavelength, the right-hand side is the wave energy dissipation zone of two wavelengths. The water depth is constant at 0.5 m.

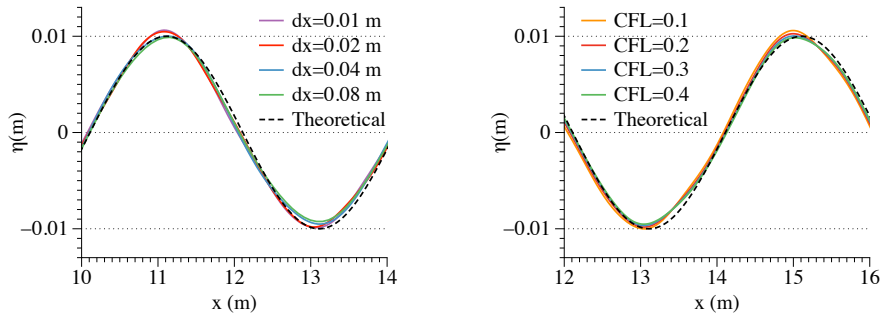


(a) Grid convergence study

(b) Time step convergence study

Figure 3: The convergence study of the linear progressive wave simulation in a 1D wave flume with REEF3D::SFLOW: (a) grid convergence study (CFL number is kept constant 0.2), (b) time step convergence study.

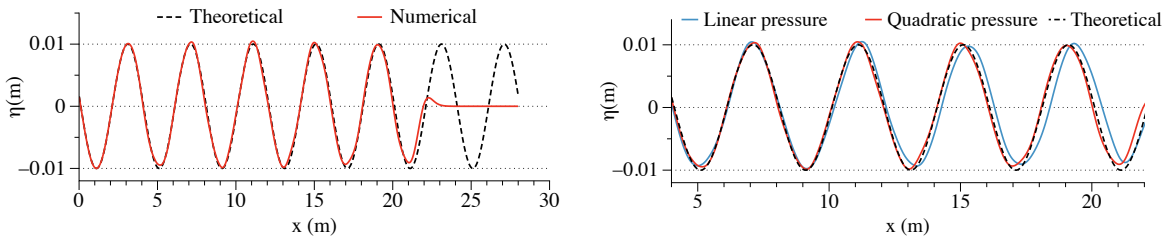


(a) (b)

Figure 4: The wave surface elevation profiles at $t = 90$ s with a linear wave of wave height $H = 0.02$ m, wavelength $L = 4$ m, cell size $dx = 0.02$ m and $CFL = 0.2$: (a) quadratic pressure approximation in the vertical direction; (b) comparison between quadratic pressure approximation and linear pressure profile in the vertical direction.

Table 1: The spatial discretisation error analysis for the progressive linear wave simulation.

| dx (m) | $\overline{H}$ (m) | relative error | L2 error |
|---|---|---|---|
| 0.08 | 0.0186 | -7.00 % | 0.0046 |
| 0.04 | 0.0193 | -3.50 % | 0.0023 |
| 0.02 | 0.0196 | -2.00 % | 0.0014 |
| 0.01 | 0.0197 | -1.50% | 0.0010 |

Table 2: The CFL error analysis for progressive linear wave simulation.

| CFL | $\overline{H}$ (m) | relative error | L2 error |
|---|---|---|---|
| 0.4 | 0.0192 | -4.00 % | 0.0024 |
| 0.3 | 0.0194 | -3.00 % | 0.0019 |
| 0.2 | 0.0196 | -2.00 % | 0.0014 |
| 0.1 | 0.0197 | -1.50% | 0.0009 |

### 3.2 $2^{nd}$-order Stokes wave propagation over constant bathymetry

Next, a $2^{nd}$-order Stokes wave Dean and Dalrymple (1991*b*) of $H = 0.1$ m and $L = 4$ m is simulated in the same 1D numerical flume. The grid convergences study is presented in Fig. 5a. Similar to the previous study, the cell size $dx = 0.02$ m is found to be suitable for this case. The average wave height of the last ten periods are again used for the convergence study. The relative errors and L2 norms of the absolute error for different grids are summarised in Table. 3. With the quadratic pressure approximation, the asymmetry due to the high-order approximation is well presented, and both, the wave height and phase match well with the theory. It shows that the model provides a good representation of the non-linearity of progressive waves. In comparison, the simulation with linear pressure profile shows an increasing difference in phase over time compared to the theoretical result.

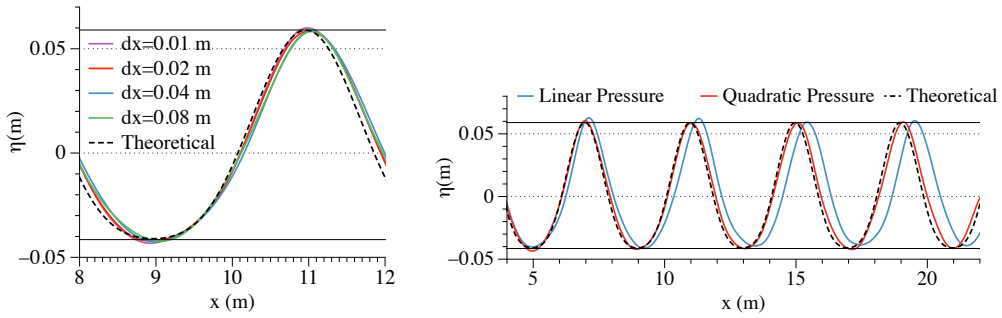


(a) (b)

Figure 5: (a) Grid convergence study for the $2^{nd}$-order Stokes progressive wave with the wave height $H = 0.1$ m, the wavelength $L = 4$ m and $CFL = 0.2$. (b) The wave surface elevation profile at $t = 90$ s with the cell size $dx = 0.02$ m. The two horizontal solid black lines represent the theoretical wave envelope.

Table 3: The spatial discretisation error analysis for progressive $2^{nd}$-order Stokes wave simulation.

| dx (m) | $\overline{H}$ (m) | relative error | L2 error |
|---|---|---|---|
| 0.08 | 0.0957 | -4.30 % | 0.0136 |
| 0.04 | 0.0991 | -0.90 % | 0.0030 |
| 0.02 | 0.1003 | 0.30 % | 0.0010 |
| 0.01 | 0.1011 | 1.10 % | 0.0035 |

### 3.3 Cnoidal wave propagation over constant bathymetry

A $5^{th}$-order cnoidal wave Korteweg and de Vries (1895); Dean and Dalrymple (1991*b*) of $H = 0.21$ m and $L = 4$ m is investigated in the 1D numerical flume to test steep periodic wave propagation in shallow water. The steepness of the wave is $H/L = 0.0525$, the wave length to depth ratio is $H/d = 0.42$ which is about 65% of the breaking limit suggested by Laitone (1960). As shown in Fig. 6a, $dx = 0.02$ m is still a suitable cell size to capture the wave surface elevation accurately despite the increased wave steepness. Following the same methodology as in section 3.1, the relative error and L2 norms are computed and shown in Table 4. The wave profiles obtained with the quadratic pressure approximation and the linear pressure assumption are also compared in Fig. 6b. The wave troughs start to show slight deformation while the crests are still well preserved with the wave height to depth ratio closer to the breaking limit. The geometry of the steep cnoidal wave is kept constant during the propagation. It is also observed that the phase misalignment from the linear pressure assumption amplifies with the increase of wave steepness because the linear pressure profile assumption deviates further from the physical pressure distribution.

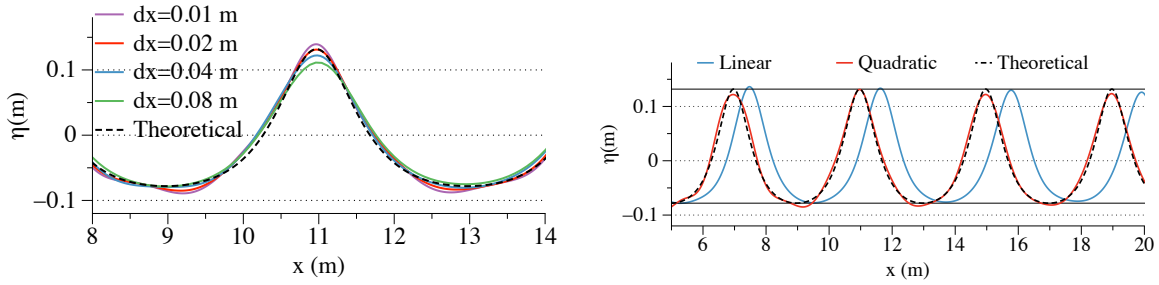


(a) (b)

Figure 6: (a) The grid convergence study for the $5^{th}$-order cnoidal progressive wave with the wave height $H = 0.21$ m, the wavelength $L = 4$ m and $CFL = 0.2$. (b) The wave surface elevation profile at $t = 90$ s with the cell size $dx = 0.02$ m. The two horizontal solid black lines represent the theoretical wave envelope.

Table 4: The spatial discretisation error analysis for progressive cnoidal wave simulation.

| dx (m) | $\overline{H}$ (m) | relative error | L2 error |
|---|---|---|---|
| 0.08 | 0.1719 | -18.14 % | 0.0978 |
| 0.04 | 0.1958 | -6.76 % | 0.0449 |
| 0.02 | 0.2047 | -2.52 % | 0.0168 |
| 0.01 | 0.2110 | 0.48 % | 0.0031 |

### 3.4 Solitary wave propagation over constant bathymetry

A solitary wave Munk (1949); Dean and Dalrymple (1991*b*) propagation over a constant bathymetry is simulated for 60 s in a 1D flume of 100 m length. The input wave height is is $H = 0.05$ m, and the constant water depth is $d = 0.5$ m. A wave generation zone of 4 m and a wave energy dissipation zone of 8 m are allocated at the inlet and the outlet of the flume. The comparison of the wave profiles at $t = 90$ s simulated with different grids is shown in Fig. 7a. The relative errors and L2 norms are also computed and shown in Table 5.

Further, simulations with the quadratic pressure approximation and the linear pressure assumption are simulated with $dx = 0.02$ m. The numerical computations are compared to the analytical values at propagation time 10 s, 20 s, 30 s and 40 s, shown in Fig. 7b. It is seen that the numerical results with the quadratic pressure remain in good agreement during the entire wave propagation process. Small amplitude waves propagate in opposite direction and trailing waves start to form during the simulation with the linear pressure. Simultaneously, the wave height increases during the process due to weaker dispersion from the linear assumption. These findings are in agreement with the investigations of Jeschke et al. (2017).

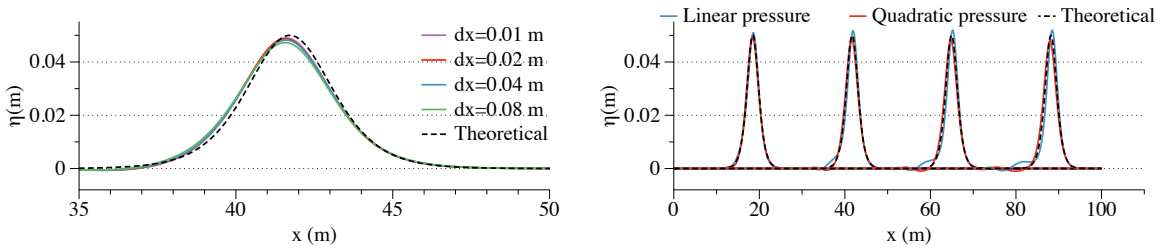


(a) (b)

Figure 7: (a) The grid convergence study for the solitary wave propagation with the wave height $H = 0.05$ m, the wavelength $L = 100$ m and $CFL = 0.2$. (b) Comparison of the analytical surface elevation of the solitary wave with the simulation results of the quadratic and linear vertical pressure profile after a propagation time of 10 s, 20 s, 30 s and 40 s (from left to right).

Table 5: The spatial discretisation error analysis for progressive solitary wave simulation.

| dx (m) | $\overline{H}$ (m) | relative error | L2 error |
|---|---|---|---|
| 0.08 | 0.0473 | -5.40 % | 0.0027 |
| 0.04 | 0.0483 | -3.40 % | 0.0017 |
| 0.02 | 0.0487 | -2.60 % | 0.0013 |
| 0.01 | 0.0490 | -2.00 % | 0.0010 |

The model's scaling capacity is investigated by conducting a series of simulations for 500 time step iterations with the number of processors being 16, 32, 64, 128, 256 and 512 on the supercomputer Vilje. The dimension of the computational domain is (10000 m $\times$ 1000 m $\times$ 10 m). The input wave is a $2^{nd}$-order Stokes wave of wave height $H = 5$ m and wavelength $L = 100$ m. A cell size of $dx = 1$ m is used, resulting in 10 million cells in total. It is empirically assumed that the scaling is linear within 16 processors, i.e. one physical node on the cluster. Therefore, the computation time with one processor is linearly extrapolated from the 16-processor simulation. The computational speed of the one-processor simulation is considered as the base reference. The simulation time on one processor divided by the simulation time on multiple processors is defined as a speed-up factor. The relation between the speed-up factor and the number of processors as well as the number of cells per processor are plotted in Fig. 8. It shows that the performance increases almost linearly with the number of processors within the chosen range.

# 4 Validations and Applications

The evolution of waves over a non-constant bathymetry is complicated, and the performance gain from the quadratic pressure approximation in a general setting was recommended as future work by Jeschke et al. (2017). To fill the research gap, wave propagations over non-constant bathymetries of various configurations are simulated and validated with the available experimental data. A wave-structure interaction study is also validated against the bench-

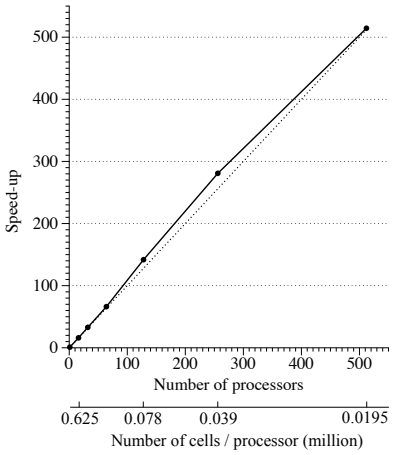


Figure 8: The performance of the parallel computation, shown as a relation between the speed-up factor in reference to the single-processor simulation for 500 iterations versus the number of processors and the number of cells per processor

mark. Jeschke et al. (2017) suggest the quadratic pressure approximation has the best performance when the water depth to wave length ratio is below 0.25. The selected benchmark cases all share the water depth condition within the suggested range. In addition, a large-scale wave propagation over a natural topography is presented based on an engineering scenario.

### 4.1 Wave propagation over a submerged bar

First, the well-known benchmark case of wave propagation over a submerged bar Beji and Battjes (1993) is tested. The configuration of the numerical set-up based on the experiment is shown in Fig. 9. A 2D wave tank of 38 m is equipped with a wave generation zone of 5 m to the left end and a wave energy dissipation zone of 9.5 m to the right end. The beginning of the submerged bar is located 6 m downstream from the wave generation zone. Eight wave gauges are located above the submerged bar with the x-coordinates being 11 m, 16 m, 17 m, 18 m, 19 m, 20 m, 21 m and 22 m, as shown in Fig. 9. The incident wave height is $H = 0.021$ m, and the wave period is $T = 2.525$ s. A grid convergence study is performed at gauge 2 and 6, before and after the crest of the submerged bar, as shown in Fig. 10i and Fig. 10j. A cell size of $dx = 0.02$ m is found to sufficiently represent the phenomena and shows good agreement with the experimental data. A simulation time of 60 s is used.

The numerically predicted time series of the surface elevations at gauge 1 to gauge 8 are compared with the experimental data in Fig. 10. The results match well with the experimental measurements before the waves reach the submerged bar and during the shoaling process, for example at gauges 1 and 2. It demonstrates that the model can represent the dispersion relations well with changing bathymetry. At the crest of the bar, no wave breaking happens but the wave decomposition takes place and results in higher harmonic wave components. The wave decomposition phenomenon is observed at wave gauges 3 to 5, where the numerical results show accurate agreement with the experimental measurements as well. On top of the relatively steep downslope, the waves undergo a de-shoaling process as the water depth increases. During this process, it is observed that the numerical results start to show differences

in phase from the experimental data. The discrepancies accumulate from wave gauge 6 to wave gauge 7. When the waves reach wave gauge 8, a significant difference is observed. This shows a less discussed limitation of existing shallow water approximations for de-shoaling processes. Furthermore, the results are also compared between the quadratic and the linear pressure profile assumptions. As an example, the comparisons of the surface elevations at gauge 3 and 5 are shown in Fig. 11. At both gauges, the quadratic assumption shows good alignment in phase with the experiment, while the linear assumption tends to predict a faster moving wave front. The observation is consistent with the investigation in section 3.

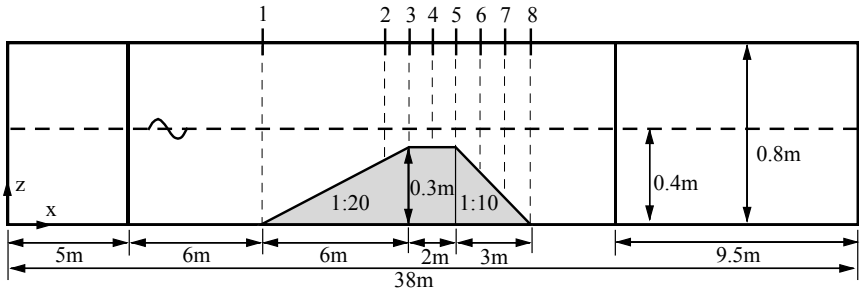


Figure 9: The numerical wave tank set-up of the wave propagation over a submerged bar, view from the side. The water depth is constant at 0.4 m. The locations of the wave elevation gauges are marked with short vertical line segments from 1 to 8. The grey-shaded object is the submerged bar. A wave generation zone of 5 m and a wave energy dissipation zone of 9.5 m are located at the left end and right end of the tank respectively.

### 4.2 Solitary wave interaction with a rectangular abutment

In this benchmark study, the solitary wave interaction with a surface-piercing rectangular abutment is investigated. Based on the experiments Higuera et al. (2013*b*); Lara et al. (2012), the numerical wave tank is defined as shown in Fig. 12. The tank is 23.86 m long, 0.58 m wide and 0.9 m deep. The still water level is constant at 0.45 m. A wave generation zone of 3.93 m is placed at the left end of the numerical wave tank to cover the effective wave length of the solitary wave Dean and Dalrymple (1991*a*), and a fully reflective wall is placed at the right end. A $3^{rd}$-order solitary wave Grimshaw (1971) with a wave height of 0.1 m is generated in the wave generation zone. The front face of the abutment is located 14.86 m from the beginning of the tank. Nine wave gauges are located upstream, sideways and downstream of the abutment, as shown in Fig. 12. For the grid convergence study, three different cell sizes $dx = 0.05$ m, 0.1 m and 0.2 m are used. All cases are simulated for 30 s to allow enough time for the reflected wave to interact with the abutment and propagate back to the generation zone.

The simulated time series at all wave gauges are compared to those from the experiments as shown in Fig. 13. The first peak in the distributions is the result of the incoming solitary wave impact on the abutment. After the incident solitary wave passes the abutment, it is reflected from the wall at the end of the tank and interact with the abutment again, resulting in the second peak. The grid convergence study shown in Fig. 13j is performed at gauge 7, which is located at the downstream side of the abutment. At this location, both, the

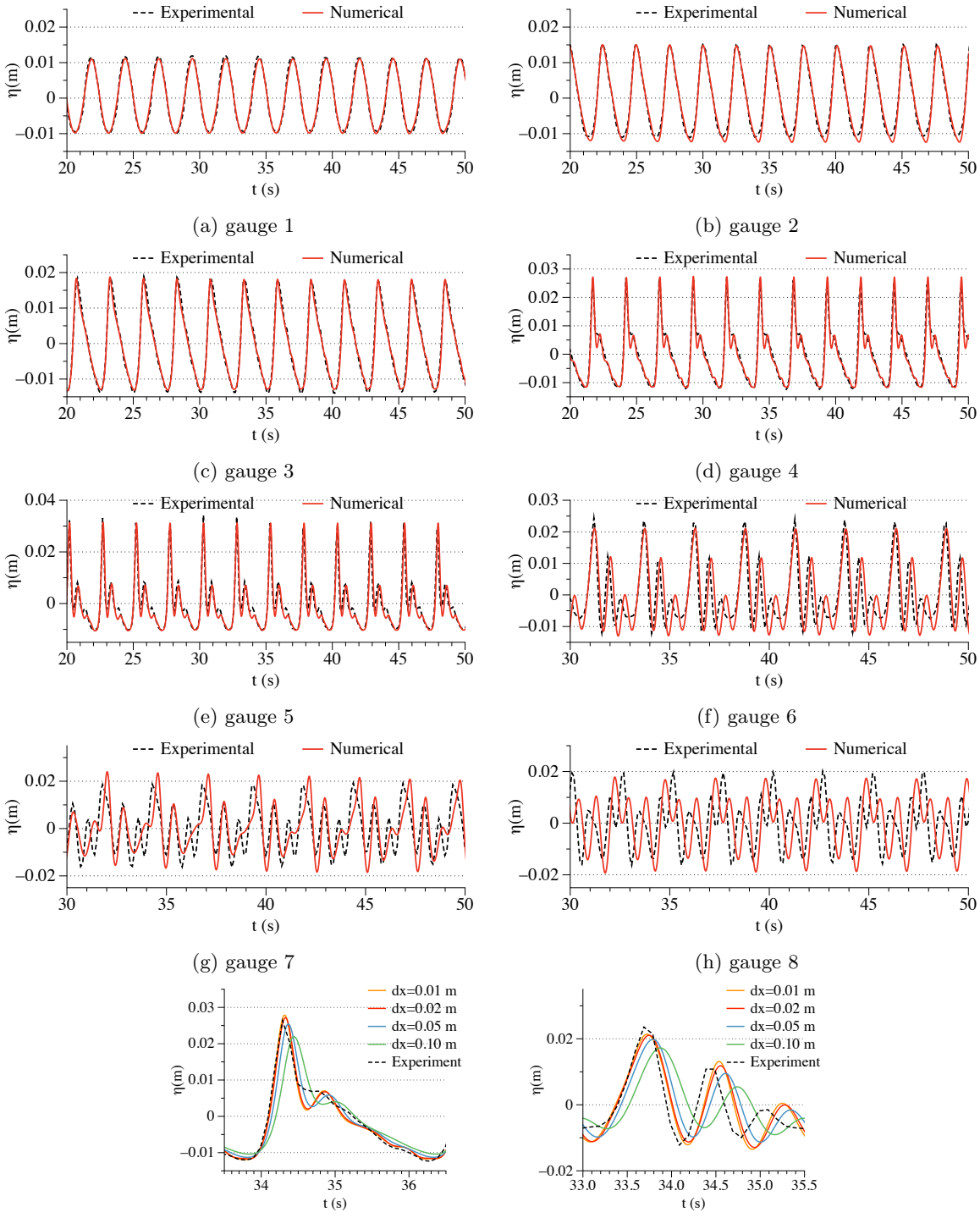


(a) gauge 1

(b) gauge 2

(c) gauge 3

(d) gauge 4

(e) gauge 5

(f) gauge 6

(g) gauge 7

(h) gauge 8

(i) Grid Convergence at the wave gauge 4

(j) Grid Convergence at the wave gauge 6

Figure 10: The surface elevations of the wave transformation over a submerged bar. (a)-(h) show the surface elevations at different wave gauges at $t = 60$ s, black lines are from laboratory experiments, red lines are results of REEF3D::SFLOW. The cell size $dx = 0.02$ m and $CFL = 0.2$. (i) and (j) are grid convergence study at wave gauge 4 and 6.

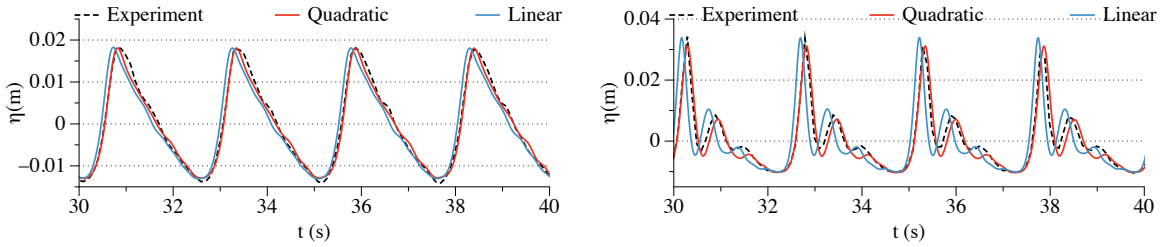


Figure 11: The comparison of the surface elevation between the quadratic and linear pressure profile assumptions at gauge 3 (a) and gauge 5 (b) in the simulation of wave propagation over a submerged bar.

interaction between the structure and the incoming waves and the properties of the reflected waves can be well observed. It indicates that the cell size $dx = 0.05$ m sufficiently captures the details of the wave pattern and gives good results compared to the experiments. At gauge 1 and 2, the first peaks show the solitary wave propagates without much interruption and, therefore, preserves its wave height. A second minor peak is noticed right after the peak which is due to the partially reflected waves from the abutment. Gauge 3 shows an increase of the wave height due to the narrowing of the channel, while gauge 4 presents a further increase of the peak because of the interaction with the abutment. The peaks increase to about 0.11 m and 0.13 m at gauge 3 and 4 respectively. Since gauge 5 is located in the constricted part of the channel, the flow velocity increases and the pressure decreases. As a consequence, the wave surface drops. At gauge 6, the first peak occurs right after the wave crest passes the abutment while the depth-averaged solution tends to smooth out the results in the sheltered region behind the abutment. At gauge 8 and 9, two peaks of equal heights are observed, indicating that the reflected wave shares the same wave height as the incoming wave. This shows that there is no damping of the soliton and the model provides an accurate representation of the solitary wave propagation. Similarly, the two peaks also share similar height at gauge 7, where no wave transformations occur before and after the wave reflects from the vertical wall. When the reflected wave reaches the abutment, a second peak occurs at gauge 6. After the reflected wave passes the abutment, gauge 4 also witnesses the second peak. In general, the wave patterns from gauge 6 and gauge 4 mirror each other.

Finally, the second peak at wave gauge 5 and the first peak at wave gauge 7 are compared with the quadratic and the linear pressure approximation in Fig. 14. Similar to the previous observations, the linear approximation predicts a increased phase velocity while the quadratic approximation matches the experiment well in phase.

The details of the free-surface during this process is also visualised in Fig. 15. Fig. 15a shows the free-surface at simulation time $t = 7$ s, right before the solitary wave reaches the abutment. The solitary wave preserves its waveform. After the wave passes the abutment, a vortex is observed at the downstream behind the abutment, as can be seen in Fig. 15b. When the reflected wave reaches back towards the abutment from the right-hand side, the wave crest meets the vortex from the last interaction before a second interaction, as seen in Fig. 15c. After the reflected wave passes the abutment, two vortices are observed on both sides of the abutment. Fig. 13 reveals that the resolution of the vortex is smoothed out at gauge 4 and 6, while the other wave gauges are well represented.

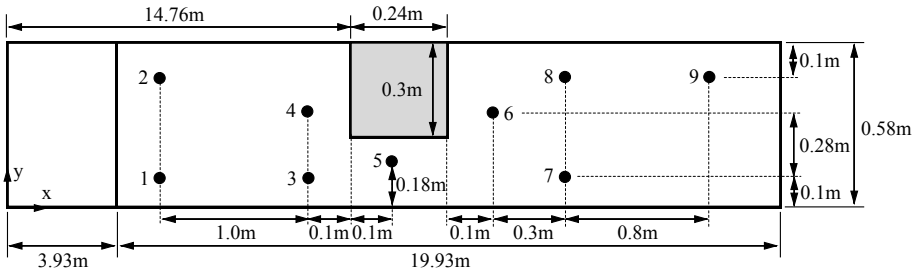


Figure 12: The numerical wave tank set-up of the solitary wave interaction with a rectangular abutment in a view from above. The grey-shaded object is the abutment. The following three groups of wave gauges share the same y-coordinate: wave gauges 1,3,7; wave gauges 4,6 and the wave gauges 2,8,9. A wave generation zone of 3.93 m is located on the left-hand side, the solid wall is located on the right-hand side to allow full reflection of the waves.

It might be interesting to notice that the 2D shallow water model is as accurate as the CFD study in Bihs et al. (2016) except for the vortices representation in the wakes of the abutment. Here, the results of simulations based on the 3D Navier-Stokes equations show a slightly better match with the experiments. The cost of the computational resource, however, is significantly lower using the proposed shallow water model. This benchmark case is simulated with 16 processors on the Vilje supercomputer about 56 times faster than the 3D simulation with the same configuration.

### 4.3 Plunging breaking waves over a sloping bed

In section 4.1, non-breaking waves over a submerged bar are modelled. In a more extreme situation, where the shoaling is so strong that the wave steepness increases over a certain threshold, the wavefront becomes unstable and breaking takes place. The numerical wave tank is initialised based on the experiments in Ting and Kirby (1994, 1996) to model a breaking wave scenario. The wave tank has a total length of 40 m and a height of 1 m. A wave generation zone of 9.8 m is located at the inlet of the tank; a wave energy dissipation zone of the same length is arranged at the outlet. An inclined bed with a slope of 1:35 is located 4 m away from the wave generation zone. The obstacle increases to 0.748 m at the right end of the tank. The water depth is constant at 0.4 m. Wave gauges 1-4 are located on the slope, 10 m, 11 m, 12 m and 12.3 m away from the wave generation zone respectively. A $5^{th}$-order cnoidal wave with wave height $H = 0.128$ m and wave period $T = 5$ s is propagated in this simulation, which is supposed to result in a plunging breaker on the slope according to the experiment. A simulation time of 40 s is used.

The sensitivity to the grid resolution is investigated with different cell sizes of $dx = 0.0025$ m, $0.005$ m, $0.01$ m, $0.02$ m and $0.05$ m. The wave surface elevation at wave gauge 4 is chosen for comparing the results from different cell sizes. As can be seen in Fig. 17e, the simulations capture very steep wavefronts as well as instabilities at the wave crest with all cell sizes. It is not possible to observe the over-turning process because the shallow water model represents the free-surface with a single-valued function. Though, a vertical wavefront and instability at the wave crest indicates the breaking process. The view on the wave crest is shown in more detail in Fig. 17f, where it is visible that $dx = 0.005$ m captures the peak values

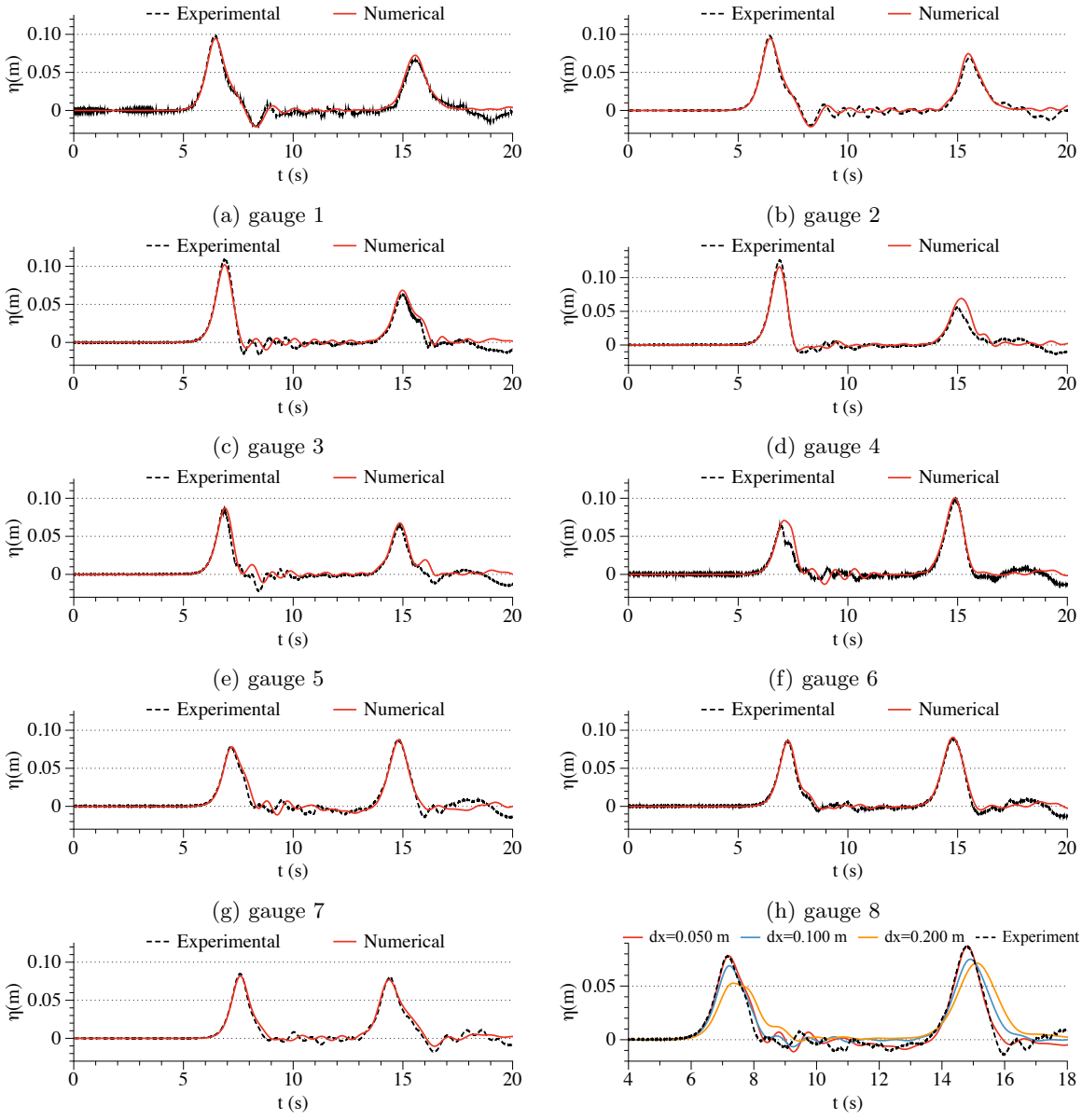


(a) gauge 1 (b) gauge 2

(c) gauge 3 (d) gauge 4

(e) gauge 5 (f) gauge 6

(g) gauge 7 (h) gauge 8

(i) gauge 9 (j) Grid Convergence Study at gauge 7

Figure 13: Wave surface elevation at the wave gauges are shown in (a)-(i). The input solitary wave has a wave height of $H = 0.1$ m. The black dashed lines are from laboratory experiments, red solid lines are results from REEF3D::SFLOW. The cell size is $dx = 0.05$ m and $CFL = 0.2$ is used. (j) shows the grid convergence study.

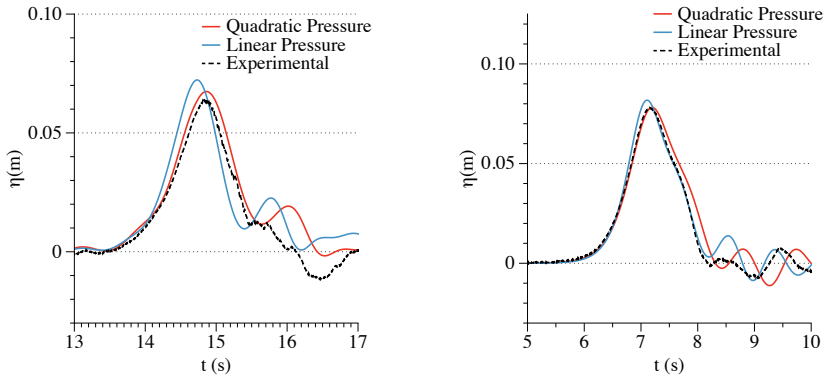


(a) (b)

Figure 14: The comparison of the surface elevation between the quadratic and linear pressure profile approximation at gauge 5 (a) and gauge 7 (b) in the simulation of solitary wave interaction with a rectangular abutment.

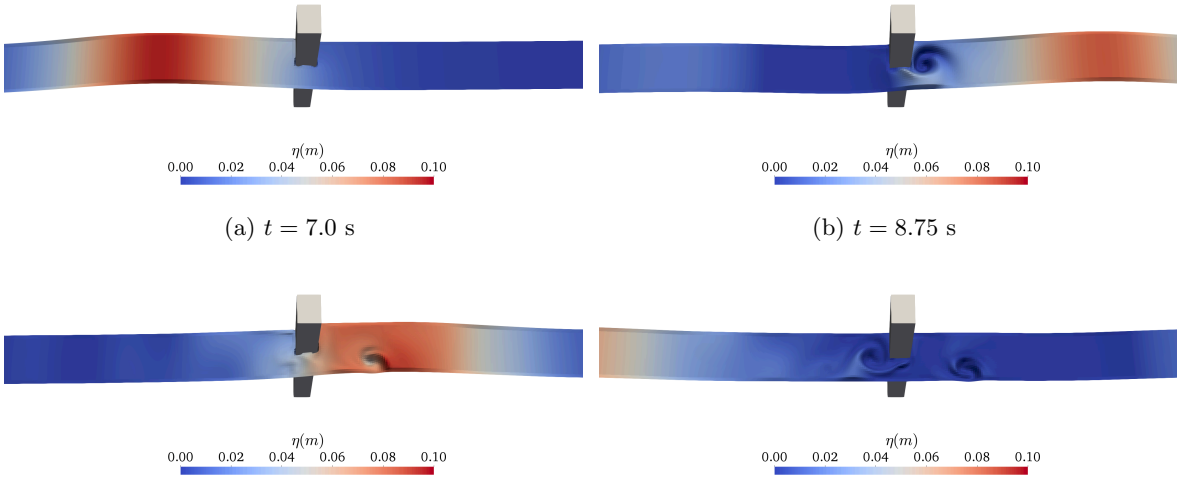


(a) $t = 7.0$ s (b) $t = 8.75$ s

(c) $t = 15.25$ s (d) $t = 17.5$ s

Figure 15: Surface elevation of the input and reflected wave interaction with the rectangular abutment, (a) right before the input solitary wave reaches the abutment, (b) right after the input solitary wave passes the abutment, (c) right before the reflected wave reaches the abutment from the right-hand side, (d) right after the reflected wave passes the abutment.

most accurately. The simulated wave elevations at different wave gauges with $dx = 0.005$ m are compared to the experimental data in Fig. 17 in order to assess the model's capacity to resolve the surf-zone wave transformations. The wave crests increase significantly when the waves propagate from gauge 1 to gauge 2, showing an increasing shoaling process. As the waves evolve on the slope, an unstable wave crest is seen at gauge 3 and the wave height decreases slightly compared to that at gauge 2. The instability at the crest remains as the waves approach gauge 4 and a further decrease of the wave crest is noticed. These time series suggest that the breaking happens between gauge 2 and 3. To identify the breaking point, the wave elevation profile at different time are compared in the same plot (Fig. 18). It is seen that at $x = 21.580$ m, the wave crest is the highest while the wavefront becomes vertical for the first time indicating the location of the breaking point. Correspondingly, a breaking height of $h_b = 0.208$ m is measured at $x = 21.580$ m. In the experiment, the breaking point is detected at $x = 21.595$ m and a breaking height of $h_b = 0.196$ m is measured. Both, the predicted breaking point and are very close to that in the experiment. The wave surface elevation profile is illustrated in Fig. 19. As can be seen in Fig. 19a, the wave height increases significantly, the wave shape becomes narrower, the crest becomes unstable and the wavefront becomes vertical, indicating a breaking process. At a later time, the wave energy dissipates and the wave height decreases dramatically. An attempt to simulate the breaking wave using the linear pressure approximation leads to a numerical failure. It indicates that the quadratic pressure approximation is superior for the simulation of breaking waves.

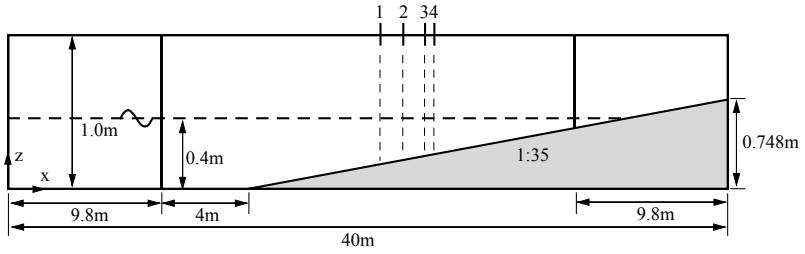


Figure 16: The numerical wave tank set-up of the wave breaking over a sloping bed, view from the side. The water depth is constant at 0.5 m, the grey-shaded object is the sloping bed with a slope of 1:35. Four wave gauges are arranged near the breaking point.

## 4.4 Large scaling numerical modelling of coastal waves near Mehamn harbour

The previous benchmark studies have quantitatively examined the capacities of the proposed model. In this section, the wave propagation in a large domain with real topography is simulated to show the model's computational efficiency and its capacity for operational engineering applications. The chosen scenario is Mehamn harbour in northern Norway, highlighted by a black box in Fig. 20. The harbour is the north-most Hutigruten harbour and it is connected to the open sea to the north and relatively well protected from the west and the east. The bathymetry outside the harbour has a mostly intermediate water depth condition with moderate changes of topography. The computational domain is 10.5 km in the east-west direction and 14 km in the north-south direction, with the deepest water depth being 147.5 m. The

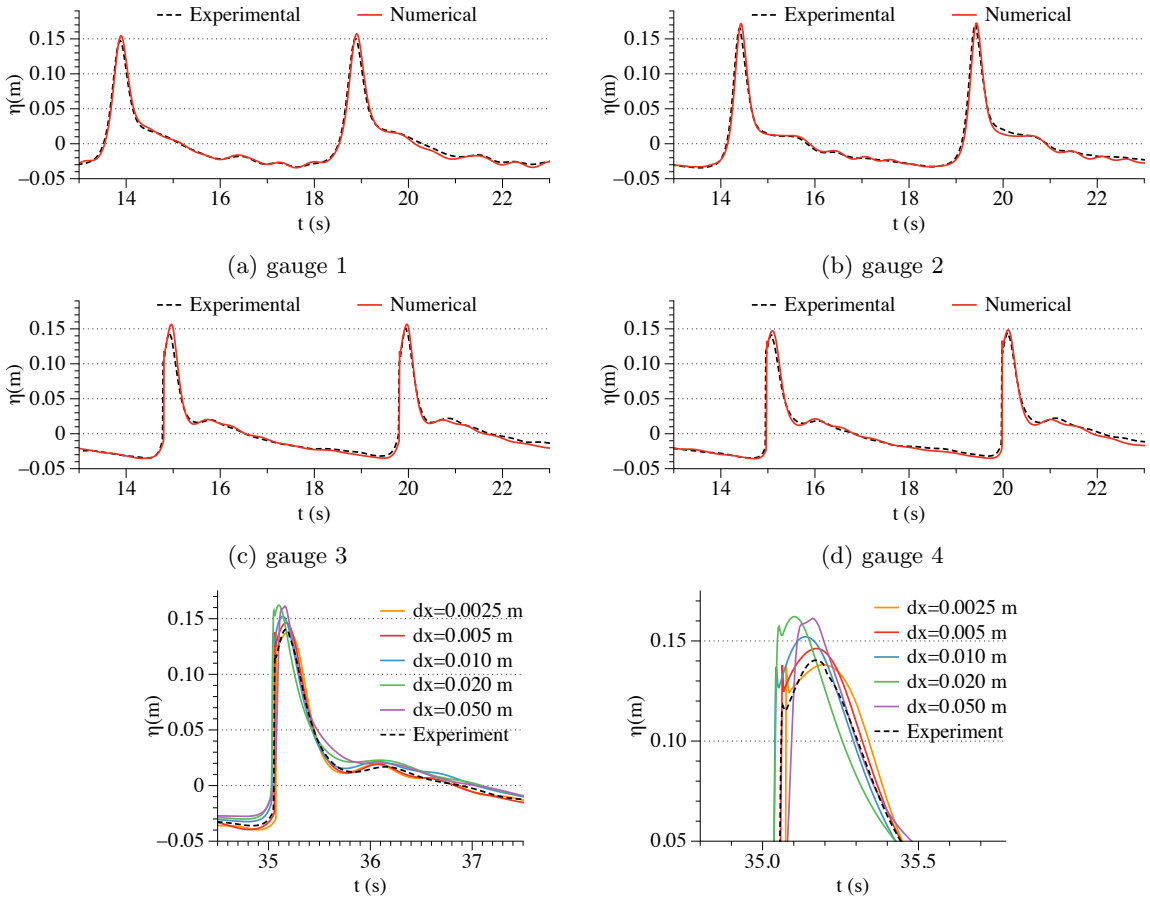


(a) gauge 1

(b) gauge 2

(c) gauge 3

(d) gauge 4

(e) Grid convergence study at gauge 4

(f) Grid convergence study at gauge 4 with the wave crest zoomed in

Figure 17: Wave surface elevations of wave breaking over a sloping bed. The input wave is a $5^{th}$-order cnoidal wave with a wave height of $H = 0.128$ m and a wave period of $T = 5$ s. The cell size is $dx = 0.005$ m and $CFL = 0.2$ is used. Black dashed lines are from laboratory experiments, red solid lines are results from REEF3D::SFLOW.

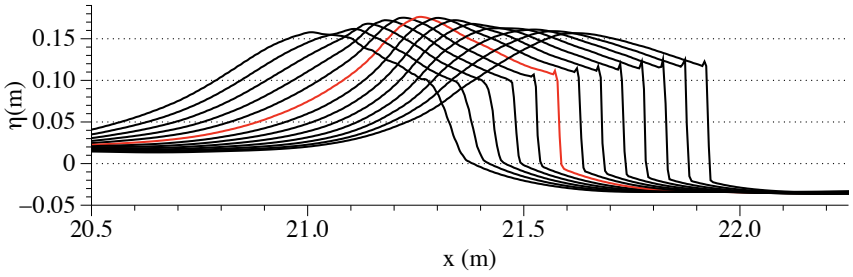


Figure 18: The wavefront evolution near the wave breaking point, from the numerical simulation with $dx = 0.005$ m. When the wavefront turns vertical for the first time, shown as a red curve, the breaking and overturning process starts.

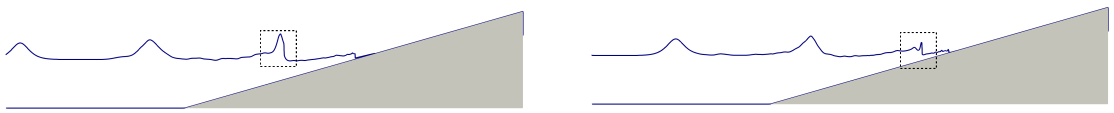

(a) (b)

Figure 19: The wave surface elevation profiles along the x-direction. (a) the breaking wave at $t = 34.75$ s, as highlighted by a box of a dashed frame. (b) after the wave breaking, at $t = 37.50$ s, the wave height reduces and the wave keeps running up the sloping bed, as highlighted by a box of dashed lines.

site is exposed to swell from the open sea. An estimated regular wave of height $H = 4.5$ m and period $T = 15$ s is generated at the northern boundary. The wetting and drying scheme over the complex bathymetry is included. A cell size of 5 m is used in the simulation, resulting in 5.88 million cells. In the case of a 3D simulation with Navier-Stokes solver, such a configuration will result in 246.96 million cells assuming a uniform grid. This simulation of wave propagation in Mehamn harbour takes about 4.2 hours for 1000 s simulation time with 256 cores on the Vilje supercomputer.

The wave surface elevation at simulation time $t = 650$ s is shown in Fig. 21b. Strongly reflected waves can be seen at the tips of the peninsulas that reach out northwards into the ocean. Stripes of submerged reefs in the north-south directions create strong shoaling, as higher waves are shown to be following the same pattern of the submerged reefs. When the waves propagate southwards, refraction occurs and bend the wave rays towards the shore. When the waves start to reach the harbour, the narrowing entry causes diffraction. A fraction of the diffracted waves manages to bypass the curve-shaped peninsulas and enter the inner harbour. The complicated wave transformations and their interactions are well demonstrated in the simulation results.

Finally, the model's computational performance including a complicated bathymetry with wetting and drying and the breaking algorithm is determined in a similar manner as described in section 2. The simulations are conducted for 500 iterations with the number of processors fixed to 16, 32, 64, 128, 256 and 512 on the supercomputer Vilje. The computational time with one processor is linearly extrapolated from the 16-processor simulation and is used as a base reference for the speed-up factor. The relation between the speed-up factor and the number of processors as well as the number of cells per processor are then plotted in Fig. 22. It shows that with the presence of a complex topography and the wetting-drying scheme, the model is as computationally efficient as with a constant bottom within 200 processors, while it slows down compared to the ideal scaling characteristics afterwards.

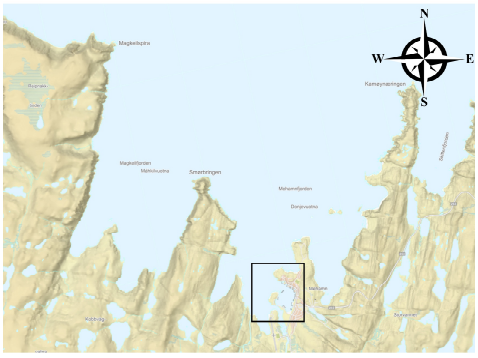


Figure 20: The illustration of the simulated region outside Mehamn harbour in northern Norway. The harbour is highlighted by a black box.

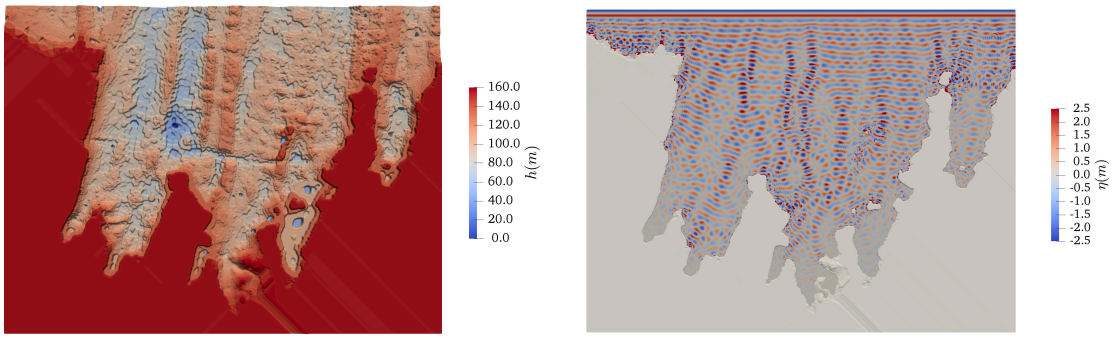


(a) (b)

Figure 21: The wave propagation towards the Mehamn harbour in the numerical simulation with a $2^{nd}$-order Stokes wave of wave height $H = 4.5$ m and wave period $T = 15$ s. The cell size is $dx = 5.0$ m and $CFL = 0.2$ is used. (a) The topography in the simulation; (b) The surface elevation at simulation time $t = 650$ s.

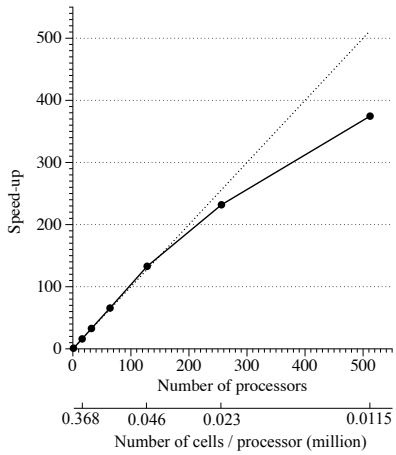


Figure 22: The performance of the parallel computation, shown as a relation between the speed-up factor in reference to the single-processor simulation for 500 iterations versus the number of processors and the number of cells per processor

# 5 Conclusion

The shallow water model REEF3D::SFLOW has been presented in this paper. The model solves the depth-averaged shallow water equations with non-hydrostatic extensions and a quadratic vertical pressure profile approximation Jeschke et al. (2017). In comparison to well-known Boussinesq-type models, the proposed model treats the pressure terms differently. A typical Boussinesq model adds higher-order terms to express the hydrodynamic pressure. The proposed model adds non-hydrostatic extensions to the shallow water equations and solves for the hydrodynamic pressure explicitly from a Poisson equation. This equation is solved iteratively using an implicit scheme. Thus, the proposed model offers simpler numerics and indicates higher numerical stability by avoiding the high-order pressure terms of a Boussinesq model. The current model assumes a quadratic pressure approximation for a better representation of dispersion and always solves the depth-averaged pressure. This is in contrast to the multi-layer approach that uses vertical layers to represent dispersion and solves the pressure at the lower layer interface. Thereby, the presented approach saves the additional computational costs from the increasing number of layers.

High-order numerical methods are incorporated into the new model. Consequently, it is the first model with the quadratic pressure approximation that combines high-order schemes and fully parallelised computation. The wave generation and absorption are achieved using a relaxation method, which is absent in the current literature. The approach proves to generate various wave types with correct amplitude and dispersion, and no artificial reflections are observed in the numerical wave tank. The accuracy of the high-order scheme is confirmed for 1D and 2D wave propagation cases with a constant bathymetry. The 2D large-scale simulation of a wave propagation over constant bathymetry presents a near-linear scaling of the computational speed with an increasing number of processors up to 512. Further, the model shows an almost linear scaling up to 128 processors if a natural topography is included in the numerical wave tank. The speed-up is reduced with a further increase of computational

units due to the complex boundary treatment from the topography.

Overall, the study confirms the advantage of the quadratic pressure approximation over the linear pressure assumption for multiple validation cases. The linear pressure assumption leads to an overshooting phase velocity for all the regular wave tests in the manuscripts. It also causes a secondary wave during the solitary wave propagation. The quadratic pressure approximation improves the phase information for progressive waves significantly and removes the unrealistic free-surface disturbances.

A key advancement presented in the current work is the inclusion of the varying bathymetry and structures in a non-hydrostatic shallow water model with the quadratic pressure approximation. A fractional step method is applied in the proposed numerical model in order to meet the challenge of incorporating the term $\Phi$ that appears in the bottom pressure calculation. Thus, the simulations of the nonlinear long wave propagation over varying topographies using a non-hydrostatic model with the quadratic pressure assumption are possible for the first time. The wave transformations over varying topography are well represented and in good agreement with the experimental data. The model can represent the complex free-surface during wave-structure interactions and predicts the breaking wave height and locations accurately. The quadratic pressure approximation again provides a better representation of the free-surface than the linear pressure assumption for the wave propagation over varying bathymetries. The challenges of representing the de-shoaling process using a non-hydrostatic shallow water model is also discussed, and the study confirms the findings from previous research Dingemans (1994).

It can be concluded that, within the applicable range of the quadratic assumption Jeschke et al. (2017), the quadratic pressure approximation presents better results both with a constant and a varying bathymetry. The large-scale engineering application shows a good computational scaling character with the wetting and drying of complex topography included. In general, the model presents itself as a good alternative to shallow water modelling with robust and efficient numerical methods. The model also serves as an additional option within the hydrodynamics code REEF3D. As a consequence, an integrated wave modelling cascade is more easily adaptable because different sub-models are developed on a single platform and the information exchange can be made more convenient.

## Acknowledgements

This study has been carried out under the E39 fjord crossing project (No. 304624), and the authors are grateful to the grants provided by the Norwegian Public Roads Administration. This study was supported in part with the computational facility Vilje (https://www.sigma2.no /content/vilje) at the Norwegian University of Science and Technology (NTNU) provided by The Norwegian Metacenter for Computational Sciences (NOTUR, http://www.notur.no) under project no. NN2620K.

## References

(2015). *hypre high performance preconditioners - User's Manual*. Center for Applied Scientific Computing, Lawrence Livermore National Laboratory.

Aggarwal, A., Pákozdi, C., Bihs, H., Myrhaug, D. and Alagan Chella, M. (2018). Free surface reconstruction for phase accurate irregular wave generation. *Journal of Marine Science and Engineering*, **6**(3). ISSN 2077-1312. 10.1002/fld.480710.3390/jmse6030105.

Ahmad, N., Bihs, H., Myrhaug, D., Kamath, A. and Øivind A. Arntsen (2018). Three-dimensional numerical modelling of wave-induced scour around piles in a side-by-side arrangement. *Coastal Engineering*, **138**, 132 – 151. ISSN 0378-3839. 10.1002/fld.4807https://doi.org/10.1016/j.coastaleng.2018.04.016.

Altomare, C., Domínguez, J., Crespo, A., González-Cao, J., Suzuki, T., Gómez-Gesteira, M. and Troch, P. (2017). Long-crested wave generation and absorption for sph-based dualsphysics model. *COASTAL ENGINEERING*, **127**, 37–54. ISSN 0378-3839.

Ashby, S.F. and Flagout, R.D. (1996). A parallel mulitgrid preconditioned conjugate gradient algorithm for groundwater flow simulations. *Nuclear Science and Engineering*, **124**(1), 145–159.

Azimi, A.H., Rajaratnam, N. and Zhu, D.Z. (2014). Submerged flows over rectangular weirs of finite crest length. *Journal of Irrigation and Drainage Engineering*, **140**(5), 06014001–1 –06014001–12.

Beji, S. and Battjes, J.A. (1993). Experimental investigation of wave propagation over a bar. *Coastal Engineering*, **19**, 151–162.

Bihs, H., Kamath, A., Alagan Chella, M., Aggarwal, A. and Arntsen, Ø.A. (2016). A new level set numerical wave tank with improved density interpolation for complex wave hydrodynamics. *Computers & Fluids*, **140**, 191–208.

Chen, Q., Kirby, J.T., Dalrymple, R.A., Shi, F. and Thornton, E.B. (????). Boussinesq modeling of longshore currents. *Journal of Geophysical Research: Oceans*, **108**(C11). 10.1002/fld.480710.1029/2002JC001308.

Chorin, A. (1968). Numerical solution of the Navier-Stokes equations. *Mathematics of Computation*, **22**, 745–762.

Chow, A.D., Rogers, B.D., Lind, S.J. and Stansby, P.K. (2019). Numerical wave basin using incompressible smoothed particle hydrodynamics (isph) on a single gpu with vertical cylinder test cases. *Computers & Fluids*, **179**, 543 – 562. ISSN 0045-7930. 10.1002/fld.4807https://doi.org/10.1016/j.compfluid.2018.11.022.

Cui, H., Pietrzak, J. and Stelling, G. (2014). Optimal dispersion with minimized poisson equations for non-hydrostatic free surface flows. *Ocean Modelling*, **81**, 1 – 12. ISSN 1463-5003. 10.1002/fld.4807https://doi.org/10.1016/j.ocemod.2014.06.004.

Dalrymple, R. and Rogers, B. (2006). Numerical modeling of water waves with the sph method. *Coastal Engineering*, **53**(2), 141 – 147. ISSN 0378-3839. 10.1002/fld.4807https://doi.org/10.1016/j.coastaleng.2005.10.004. Coastal Hydrodynamics and Morphodynamics.

Dean, R. and Dalrymple, R. (1991*a*). *Water Wave Mechanics for Engineers and Scientists*. Advanced series on ocean engineering. World Scientific. ISBN 9789810204211.

Dean, R.G. and Dalrymple, R.A. (1991*b*). *Water Wave Mechanics for Engineers and Scientists*. WORLD SCIENTIFIC. 10.1002/fld.480710.1142/1232.

Dingemans, M.W. (1994). Comparison of computations with Boussinesq-like models and laboratory measurements. *Igarss 2014*, 1–30. ISSN 13514180. 10.1002/fld.480710.1007/s13398-014-0173-7.2.

Grimshaw, R. (1971). The solitary wave in water of variable depth. part 2. *Journal of Fluid Mechanics*, **46**(3), 611–622. 10.1002/fld.480710.1017/S0022112071000739.

Hanert, E., Roux, D.Y.L., Legat, V. and Deleersnijder, E. (2005). An efficient eulerian finite element method for the shallow water equations. *Ocean Modelling*, **10**(1), 115 – 136. ISSN 1463-5003. 10.1002/fld.4807https://doi.org/10.1016/j.ocemod.2004.06.006. The Second International Workshop on Unstructured Mesh Numerical Modelling of Coastal, Shelf and Ocean Flows.

Higuera, P., Lara, L.J. and Losada, I.J. (2013*a*). Realistic wave generation and active wave absorption for Navier-Stokes models application to OpenFOAM. *Coastal Engineering*, **71**, 102–118.

Higuera, P., Lara, L.J. and Losada, I.J. (2013*b*). Simulating coastal engineering processes with OpenFOAM. *Coastal Engineering*, **71**, 119–134.

Hirt, C. and Nichols, B. (1981). Volume of fluid (vof) method for the dynamics of free boundaries. *Journal of Computational Physics*, **39**(1), 201 – 225. ISSN 0021-9991. 10.1002/fld.4807https://doi.org/10.1016/0021-9991(81)90145-5.

Jacobsen, N., Fuhrman, D. and Jørgen, F. (2012). A wave generation toolbox for the open-source cfd library: Openfoam. *International Journal for Numerical Methods in Fluids*, **70**(9), 1073–1088. ISSN 0271-2091. 10.1002/fld.480710.1002/fld.2726.

Jeschke, A. (2018). *Second Order Convergent Discontinuous Galerkin Projection Method for Dispersive Shallow Water Flows*. Ph.D. thesis, Universität Hamburg.

Jeschke, A., Pedersen, G.K., Vater, S. and Behrens, J. (2017). Depth-averaged non-hydrostatic extension for shallow water equations with quadratic vertical pressure profile: equivalence to boussinesq-type equations. *International Journal for Numerical Methods in Fluids*, **84**(10), 569–583. 10.1002/fld.480710.1002/fld.4361.

Jiang, G.S. and Shu, C.W. (1996). Efficient implementation of weighted ENO schemes. *Journal of Computational Physics*, **126**, 202–228.

Kamath, A., Bihs, H., Alagan Chella, M. and Arntsen, Ø.A. (2016). Upstream-cylinder and downstream-cylinder influence on the hydrodynamics of a four-cylinder group. *Journal of Waterway, Port, Coastal, and Ocean Engineering*. 10.1002/fld.480710.1061/(ASCE)WW.1943-5460.0000339.

Korteweg, D.J. and de Vries, G. (1895). On the change of form of long waves advancing in a rectangular canal, and on a new type of long stationary waves. *Philosophical Magazine*, **39**(240), 422–443. 10.1002/fld.480710.1080/14786449508620739.

Laitone, E.V. (1960). The second approximation to cnoidal and solitary waves. *Journal of Fluid Mechanics*, **9**(3), 430–444. 10.1002/fld.480710.1017/S0022112060001201.

Lara, J., del Jesus, M. and Losada, I. (2012). Three-dimensional interaction of waves and porous coastal structures: Part ii: Experimental validation. *Coastal Engineering*, **64**, 26 – 46. ISSN 0378-3839. 10.1002/fld.4807https://doi.org/10.1016/j.coastaleng.2012.01.009.

Le, H. and Moin, P. (1991). An improvement of fractional step methods for the incompressible navier-stokes equations. *Journal of Computational Physics*, **92**(2), 369 – 379. ISSN 0021-9991. 10.1002/fld.4807https://doi.org/10.1016/0021-9991(91)90215-7.

Lynnett, P.J. and Liu, P.L.F. (200451). Linear analysis of the multi-layer model. *Coastal Engineering*, 439–454.

Madsen, P.A., Bingham, H.B. and Liu, H. (2002). A new boussinesq method for fully nonlinear waves from shallow to deep water. *Journal of Fluid Mechanics*, **462**, 1–30. 10.1002/fld.480710.1017/S0022112002008467.

Madsen, P.A., Murray, R. and Sørensen, O.R. (1991). A new form of the boussinesq equations with improved linear dispersion characteristics. *Coastal Engineering*, **15**, 371–388.

Mayer, S., Garapon, A. and Sørensen, L.S. (1998). A fractional step method for unsteady free-surface flow with applications to non-linear wave dynamics. *International Journal for Numerical Methods in Fluids*, **28**(2), 293–315. 10.1002/fld.480710.1002/(SICI)1097-0363(19980815)28:2¡293::AID-FLD719¿3.0.CO;2-1.

Miquel, A.M., Kamath, A., Alagan Chella, M., Archetti, R. and Bihs, H. (2018). Analysis of different methods for wave generation and absorption in a cfd-based numerical wave tank. *Journal of Marine Science and Engineering*, **6**(2). ISSN 2077-1312. 10.1002/fld.480710.3390/jmse6020073.

Monteban, D. (2016). Numerical modelling of wave agitation in ports and access channels.

Munk, W.H. (1949). The solitary wave theory and its application to surf problems. *Annals of the New York Academy of Sciences*, **51**(3), 376–401. 10.1002/fld.480710.1111/j.1749-6632.1949.tb27281.x.

Nwogu, O. (1993). Alternative form of boussinesq equations for nearshore wave propagation. *Journal of Waterways, Port, Coastal, and Ocean Engineering*, **119**(6), 618–638.

Ong, M.C., Kamath, A., Bihs, H. and Afzal, M.S. (2017). Numerical simulation of free-surface waves past two semi-submerged horizontal circular cylinders in tandem. *Marine Structures*, **52**, 1 – 14. ISSN 0951-8339. 10.1002/fld.4807https://doi.org/10.1016/j.marstruc.2016.11.002.

Osher, S. and Sethian, J.A. (1988). Fronts propagating with curvature- dependent speed: algorithms based on Hamilton-Jacobi formulations. *Journal of Computational Physics*, **79**, 12–49.

Roux, D.Y.L. and Pouliot, B. (2008). Analysis of Numerically Induced Oscillations in Two-Dimensional Finite-Element Shallow-Water Models Part II: Free Planetary Waves. *SIAM Journal on Scientific Computing*. ISSN 1064-8275. 10.1002/fld.480710.1137/060650106.

Sasikumar, A., Kamath, A., Musch, O., Bihs, H. and Arntsen, Ø.A. (2018). Numerical Modeling of Berm Breakwater Optimization With Varying Berm Geometry Using REEF3D. *Journal of Offshore Mechanics and Arctic Engineering*, **141**(1), 011801. ISSN 0892-7219. 10.1002/fld.480710.1115/1.4040508.

Shi, F., Kirby, J.T., Harris, J.C., Geiman, J.D. and Grilli, S.T. (2012). A high-order adaptive time-stepping tvd solver for boussinesq modeling of breaking waves and coastal inundation. *Ocean Modelling*, **43-44**, 36 – 51. ISSN 1463-5003. 10.1002/fld.4807https://doi.org/10.1016/j.ocemod.2011.12.004.

Shu, C.W. and Osher, S. (1988). Efficient implementation of essentially non-oscillatory shock capturing schemes. *Journal of Computational Physics*, **77**, 439–471.

Stelling, G. and Zijlema, M. (2003). An accurate and efficient finite-difference algorithm for non-hydrostatic free-surface fow with application to wave propagation. *International Journal for Numerical Methods in Fluids*, **43**, 1–23.

Stelling, G.S. and Duinmeijer, S.P.A. (2003). A staggered conservative scheme for every froude number in rapidly varied shallow water flows. *International Journal for Numerical Methods in Fluids*, **43**(12), 1329–1354. 10.1002/fld.480710.1002/fld.537.

The SWASH Team (2017). SWASH User Manual version 4.01A.

Ting, F. and Kirby, J. (1994). Observation of undertow and turbulence in a laboratory surf zone. *Coastal Engineering*, **24**(1), 51 – 80. ISSN 0378-3839. 10.1002/fld.4807https://doi.org/10.1016/0378-3839(94)90026-4.

Ting, F. and Kirby, J. (1996). Dynamics of surf-zone turbulence in a spilling breaker. *Coastal Engineering*, **27**(3), 131 – 160. ISSN 0378-3839. 10.1002/fld.4807https://doi.org/10.1016/0378-3839(95)00037-2.

Wei, G. and Kirby, J.T. (1995). Time-dependent numerical code for extended boussinesq equations. *Journal of Waterway, Port, Coastal, and Ocean Engineering*, **121**(5), 251–261. 10.1002/fld.480710.1061/(ASCE)0733-950X(1995)121:5(251).

Wei, G., Kirby, J.T., Grilli, S.T. and Subramanya, R. (1995). A fully nonlinear boussinesq model for surface waves. part 1. highly nonlinear unsteady waves. *Journal of Fluid Mechanics*, **294**, 71–92. 10.1002/fld.480710.1017/S0022112095002813.

Zijlema, M. and Stelling, G. (2008). Efficient computation of surf zone waves using the nonlinear shallow water equations with non-hydrostatic pressure. *Coastal Engineering*, **55**(780–790).

Zijlema, M., Stelling, G. and Smit, P. (2005). Further experiences with computing non-hydrostatic free-surface flows involving water waves. *International Journal for Numerical Methods in Fluids*, **48**, 169–197.

Zijlema, M., Stelling, G. and Smit, P. (2011*a*). SWASH: An operational public domain code for simulating wave fields and rapidly varied flows in coastal waters. *Coastal Engineering*, **58**, 992–1012.

Zijlema, M., Stelling, G. and Smit, P. (2011*b*). Swash: An operational public domain code for simulating wave fields and rapidly varied flows in coastal waters. *Coastal Engineering*, **58**(10), 992 – 1012. ISSN 0378-3839. 10.1002/fld.4807https://doi.org/10.1016/j.coastaleng.2011.05.015.